

Creation of ultracold $^{87}\text{Rb}^{133}\text{Cs}$ molecules in the rovibrational ground state

Peter K. Molony,¹ Philip D. Gregory,¹ Zhonghua Ji,¹ Bo Lu,¹ Michael P. Köppinger,¹
C. Ruth Le Sueur,² Caroline L. Blackley,² Jeremy M. Hutson,² and Simon L. Cornish^{1,*}

¹*Joint Quantum Centre (JQC) Durham-Newcastle, Department of Physics,
Durham University, South Road, Durham DH1 3LE, United Kingdom*

²*Joint Quantum Centre (JQC) Durham-Newcastle, Department of Chemistry,
Durham University, South Road, Durham, DH1 3LE, United Kingdom*

(Dated: November 5, 2014)

We report the creation of a sample of over 1000 ultracold $^{87}\text{Rb}^{133}\text{Cs}$ molecules in the lowest rovibrational ground state, from an atomic mixture of ^{87}Rb and ^{133}Cs , by magnetoassociation on an interspecies Feshbach resonance followed by stimulated Raman adiabatic passage (STIRAP). We measure the binding energy of the RbCs molecule to be $hc \times 3811.576(1) \text{ cm}^{-1}$ and the $|v''=0, J''=0\rangle$ to $|v''=0, J''=2\rangle$ splitting to be $h \times 2940.09(6) \text{ MHz}$. Stark spectroscopy of the rovibrational ground state yields an electric dipole moment of $1.225(3)(8) \text{ D}$, where the values in parentheses are the statistical and systematic uncertainties, respectively. We can access a space-fixed dipole moment of $0.355(2)(4) \text{ D}$, which is substantially higher than in previous work.

The quest for ultracold samples of trapped polar molecules has attracted considerable attention over the last decade [1, 2]. The permanent electric dipole moments of polar molecules give rise to anisotropic, long-range dipole-dipole interactions which can be tuned by applied electric fields [3]. This property, combined with the exquisite control of ultracold systems, offers exciting prospects in the fields of quantum controlled chemistry [4, 5], precision measurement [6–8], quantum computation [9] and quantum simulation [10, 11].

Direct cooling of molecules into the ultracold regime remains elusive, though recent demonstrations of laser cooling show great promise [12–14]. An alternative approach is to form ultracold molecules indirectly by association of pre-cooled atoms [15, 16]. To date, the most successful method has employed magnetoassociation on a Feshbach resonance [15, 17] to produce weakly bound molecules which are subsequently transferred to the rovibrational ground state by stimulated Raman adiabatic passage (STIRAP) [18]. Although this technique has been successfully applied in homonuclear Cs_2 [19] and triplet $^{87}\text{Rb}_2$ [20], experiments exploring the role of dipole-dipole interactions have been confined to the fermionic $^{40}\text{K}^{87}\text{Rb}$ molecule [21]. However, KRb molecules are unstable, as the exchange reaction $2\text{KRb} \rightarrow \text{K}_2 + \text{Rb}_2$ is exothermic [4]. This leads to significant loss of the molecules [22]. Nevertheless, the confinement of the molecules in a three-dimensional optical lattice [23] eliminates this reaction and has allowed pioneering studies of dipolar spin-exchange interactions [24].

Ground-state RbCs molecules offer an appealing alternative to KRb because both the exchange and trimer formation reactions are endothermic [25, 26]. The bosonic $^{87}\text{Rb}^{133}\text{Cs}$ molecule also offers a contrast with fermionic $^{40}\text{K}^{87}\text{Rb}$. Moreover, the large predicted electric dipole moment of 1.28 D [27] is easily aligned in the laboratory frame, meaning that only modest electric fields are required to realize significant dipole-dipole

interactions. $^{87}\text{Rb}^{133}\text{Cs}$ molecules have been formed via magnetoassociation in both Innsbruck [28, 29] and Durham [30, 31]. The Innsbruck group [32] subsequently performed detailed one- and two-photon molecular spectroscopy and, very recently, reported the transfer of molecules to the rovibrational and hyperfine ground state by STIRAP [33].

In this letter, we demonstrate STIRAP transfer of $^{87}\text{Rb}^{133}\text{Cs}$ molecules from a bound state near dissociation to the rovibrational ground state, producing a sample of over 1000 ground-state molecules. In the process we make detailed measurements of the binding energy and the splitting between the $J''=0$ and 2 rotational levels of the vibrational ground state ($v''=0$). Stark spectroscopy of both the excited and ground states is presented, leading to a precise measurement of the ground-state permanent electric dipole moment. We demonstrate a space-fixed dipole moment which is substantially larger than in previous work.

Details of the apparatus have been described in our studies of dual-species condensates [34, 35] and Feshbach spectroscopy [30, 31]. In this work we use a nearly-degenerate sample of $\sim 2.5 \times 10^5$ ^{87}Rb atoms in the $|f=1, m_f=1\rangle$ state and $\sim 2.0 \times 10^5$ ^{133}Cs atoms in the $|3, 3\rangle$ state, confined in the levitated dipole trap illustrated in Fig. 1(a) at a temperature of $\sim 300 \text{ nK}$. The near-threshold bound states of $^{87}\text{Rb}^{133}\text{Cs}$ relevant to our magnetoassociation sequence are shown in Fig. 1(b). As in [29], these states are labeled as $|n(f_{\text{Rb}}, f_{\text{Cs}})L(m_{f_{\text{Rb}}}, m_{f_{\text{Cs}}})\rangle$, where n is the vibrational label for the particular hyperfine ($f_{\text{Rb}}, f_{\text{Cs}}$) manifold, counting down from the least-bound state which has $n=-1$, and L is the quantum number for rotation of the two atoms about their center of mass. All states have $M_{\text{tot}} = 4$, where $M_{\text{tot}} = M_F + M_L$ and $M_F = m_{f_{\text{Rb}}} + m_{f_{\text{Cs}}}$.

To create weakly-bound molecules we sweep the magnetic field across a Feshbach resonance at $197.10(3) \text{ G}$ to

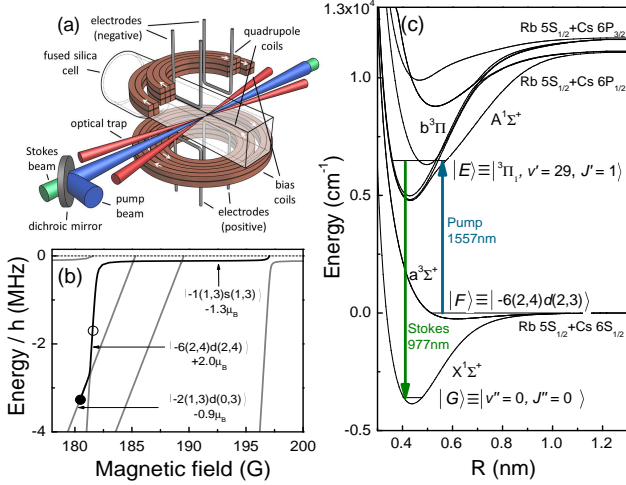


FIG. 1. (Color online) Experimental overview. (a): Simplified diagram of key elements of the apparatus. (b): Near-threshold bound states for $^{87}\text{Rb}^{133}\text{Cs}$ and the magnetoassociation path (solid black line). Stern-Gerlach separation is carried out at 180.487(4) G (closed circle) and STIRAP transfer is carried out at 181.624(1) G (open circle). An avoided crossing at ~ 181.3 G allows transfer between these two states. (c): Potential energy curves for RbCs, indicating the transitions used for STIRAP.

produce weakly-bound molecules in the $|-1(1,3)s(1,3)\rangle$ state. These molecules are then transferred to the $|-2(1,3)d(0,3)\rangle$ state at 180.487(4) G following the path shown in Fig. 1(b) and separated from the remaining atoms using the Stern-Gerlach effect [31]. To detect the molecules, we ramp back to a field above the 197.10(3) G resonance to dissociate the molecules to atoms, which are then detected by absorption imaging. We typically create trapped samples of ~ 2500 molecules in the $|-2(1,3)d(0,3)\rangle$ state with the same temperature as the original atomic sample and a lifetime of 200 ms.

We transfer the molecules from the weakly-bound state $|F\rangle$ to the ground state $|G\rangle$ by coupling them via a level $|E\rangle$ of the coupled $A^1\Sigma^+ + b^3\Pi$ manifold. This requires two lasers, labeled the pump ($\lambda = 1557$ nm) and Stokes ($\lambda = 977$ nm) lasers in Fig. 1(c). These are referenced to an optical cavity [36]. Up to 16 mW of light at each wavelength can be focused to a ~ 35 μm waist at the molecule sample. High transfer efficiency requires a high value of Ω^2/γ for both transitions, where Ω is the Rabi frequency and γ is the natural linewidth. Debatin *et al.* have identified several states suitable for STIRAP [32]. To locate the states, we pulse 20 μW of pump light, polarized parallel to the magnetic field, on the molecules in the $|F\rangle$ state for 750 μs . We observe the molecule loss as a function of optical frequency, as shown in the inset to Fig. 2, and locate the center with a Lorentzian fit. In total we have detected seven electronically-excited states and their numerous hyperfine sublevels spanning

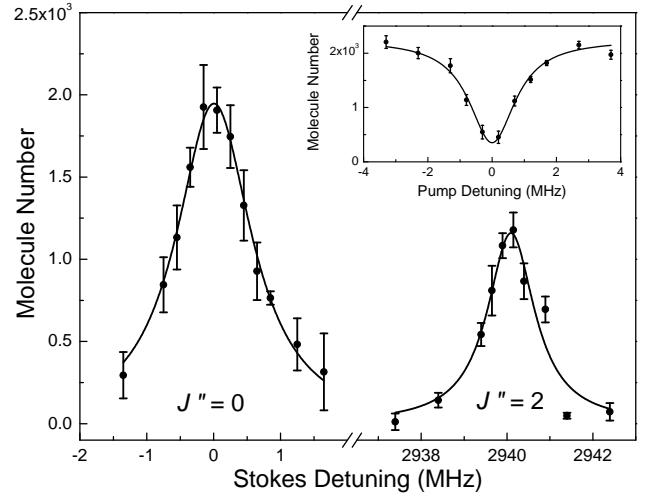


FIG. 2. Two-photon spectroscopy of the RbCs vibrational ground state. The molecules remain in the initial near-dissociation state when the Stokes light is on resonance with the $J'' = 0$ and $J'' = 2$ rotational states. The solid lines illustrate Lorentzian fits used to determine the resonance positions. Inset: One-photon loss spectrum for the $|^3\Pi_1, v' = 29, J' = 1\rangle$ state. The pump laser is held on resonance with this transition during the two-photon spectroscopy.

a 1.8 THz range. We focus on the transition to the lowest hyperfine state of the odd-parity (*e*) component of the $|^3\Pi_1, v' = 29, J' = 1\rangle$ level, which has well-separated hyperfine states and high Ω_P^2/γ [37].

To determine the pump Rabi frequency Ω_P , we set the pump laser on resonance, vary the pulse time t , and fit the fraction of remaining molecules N/N_0 to $N/N_0 = \exp(-\Omega_P^2 t/\gamma)$. We observe stronger coupling to the $|^3\Pi_1, v' = 29, J' = 1\rangle$ state from $|-6(2,4)d(2,4)\rangle$ than from $|-2(1,3)d(0,3)\rangle$. Unfortunately, the former has a positive magnetic moment and cannot be magnetically levitated in our current setup. We therefore increase the depth of the optical trap to 12.7 μK , ramp off the magnetic field gradient to transfer to an all-optical trap and adjust the bias field to transfer the molecules into $|F\rangle \equiv |-6(2,4)d(2,4)\rangle$ at 181.624(1) G (open circle, Fig. 1(b)). In this trap we observe a pump Rabi frequency of $2\pi \times 0.18(1)$ MHz at maximum power for the transition from $|F\rangle$ to $|E\rangle \equiv |^3\Pi_1, v' = 29, J' = 1\rangle$. An unlevitated trap is advantageous for STIRAP as it removes the variable Zeeman shift across the cloud. However, the transfer to the deeper trap heats the molecular cloud to 1.5(2) μK and we observe a shorter lifetime of 23(2) ms in state $|F\rangle$.

We find the Stokes transition by setting the pump laser on resonance with an increased power of 40 μW , simultaneously pulsing on 16 mW of Stokes light polarized perpendicular to the magnetic field and scanning the optical frequency. At two-photon resonance, a dark state forms

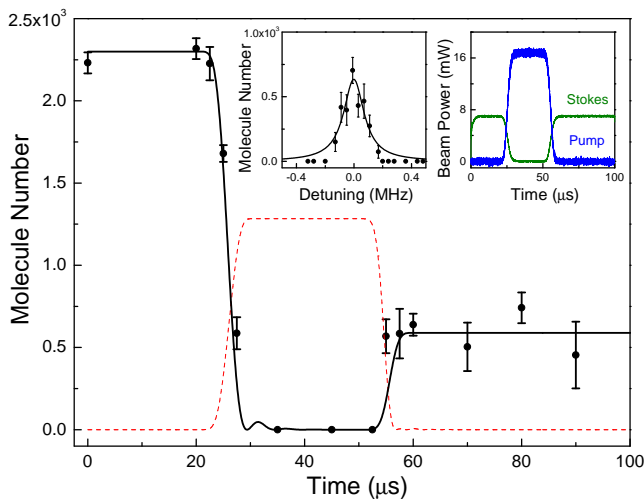


FIG. 3. (Color online) The number of molecules remaining in the Feshbach state $|F\rangle$ when both lasers are switched off during the STIRAP sequence. The black solid and red dashed lines show the Feshbach and ground-state populations obtained from the Lindblad model described in the text. Left inset: The final population of Feshbach molecules as a function of Stokes detuning. Right inset: The pump and Stokes beam powers during the STIRAP pulse sequence.

and the state $|F\rangle$ is not excited to the lossy $|E\rangle$ state. This is observed as an increase in the $|F\rangle$ state population if $\Omega_S \gg \Omega_P$, as seen in Fig. 2. We observe both the $J'' = 0$ and $J'' = 2$ levels of the electronic and vibrational ground state, separated by $h \times 2940.09(6)$ MHz. To our knowledge this is the most accurate direct measurement of this splitting. Neglecting centrifugal distortion, this implies a rotational constant $B_0 = 0.0163452(3)$ cm⁻¹, which is consistent with the theoretical prediction of $0.0163(4)$ cm⁻¹ [38]. We measure absolute frequencies of $192572.09(2)$ GHz and $306830.49(2)$ GHz for the pump and Stokes transitions respectively. This implies a zero-field binding energy of $hc \times 3811.576(1)$ cm⁻¹ for the $J'' = 0$ state, relative to the degeneracy-weighted hyperfine centers. This is consistent with the latest theoretical values [38] and experimental measurements [32].

Transfer to the ground state via STIRAP relies on a dark state $|D\rangle$ that is an eigenstate of the system on two-photon resonance. This is composed of a superposition of the $|F\rangle$ and $|G\rangle$ states, $|D\rangle = \cos \theta |F\rangle + \sin \theta |G\rangle$, where the mixing angle θ is defined by $\tan \theta = \Omega_P / \Omega_S$. Transfer from state $|F\rangle$ to $|G\rangle$ (and back) is then achieved by an adiabatic change in the mixing angle, using the pulse sequence shown in the right inset to Fig. 3. The Stokes beam is initially turned on to 7 mW for 20 μs. With $\Omega_S \neq 0$ and $\Omega_P = 0$, $|D\rangle$ is equivalent to the starting state $|F\rangle$. The Stokes beam is then ramped down in 10 μs while the pump beam is ramped up to 16 mW. This adiabatically transfers the population to the ground state

$|G\rangle$. We cannot detect the ground state directly, so after a 20 μs hold we reverse the process to transfer back to the initial state, allowing measurement of the square of the one-way efficiency. The maximum efficiency is achieved with both lasers on resonance, as shown in the left inset to Fig. 3. We map out the transfer by truncating the pulse sequence and recording the molecules remaining in the state $|F\rangle$, as shown in Fig. 3 for the on-resonance case.

The polarizations of the pump and Stokes beams drive $\Delta M_{\text{tot}} = 0$ and ± 1 transitions, respectively. The state $|F\rangle$ has $M_{\text{tot}} = 4$, so that we can reach states with $M_{\text{tot}} = 3$ or $M_{\text{tot}} = 5$. Takekoshi *et al.* [33] have shown that the transition to the $M_{\text{tot}} = 5$ hyperfine state has the strongest coupling from $|E\rangle$, with very little population transferred into the $M_{\text{tot}} = 3$ states. Furthermore, theory shows that the $I'' = 5, M_{\text{tot}} = 5$ state, where I'' is the total molecular nuclear spin, is the lowest hyperfine state at magnetic fields above about 90 G [39]. We observe only one state (left inset to Fig. 3) which we therefore conclude is the $M_{\text{tot}} = 5$ absolute ground state.

We model the transfer by numerically integrating the Lindblad master equation [36]. The maximum pump Rabi frequency of $2\pi \times 0.18(1)$ MHz is taken from one-photon measurements (see above) and both detunings are set to zero. The Stokes Rabi frequency is fitted as a free parameter and thus estimated as $2\pi \times 0.21(1)$ MHz. The results indicate a one-way transfer efficiency of 50% and the model shows that we produce ground-state ~ 1250 molecules (red dashed line in Fig. 3). The efficiency is currently limited by the Rabi frequency achieved for the pump transition. We note that a slower transfer does not increase the efficiency, because of increased laser frequency noise over longer timescales.

The permanent electric dipole moment of a polar molecule is the key quantity of interest for many applications. Without an externally applied electric field, the averaged electric dipole moment in the laboratory frame is zero. Turning on an electric field couples states of opposite parity and hence polarizes the molecules in the direction of the field. In the experiment, we apply the necessary electric field with an array of four electrodes positioned outside the fused silica cell (shown in Fig. 1(a)) [36]. We first measure the DC Stark shift of the pump transition as a function of the applied electric field. The result is shown in the upper inset in Fig. 4; the initially linear response is interrupted by an apparent avoided crossing with higher-lying hyperfine states. By following the avoided crossing, we can then measure the relative shift between the $|E\rangle$ and $|G\rangle$ states (the Stokes shift). As the electric dipole moment of the state $|F\rangle$ is negligible due to the large interatomic separation, the difference between the pump and Stokes shifts yields the DC Stark shift of the rovibrational ground state (shown in Fig. 4).

We fit the Stark shift by calculating the matrix solution

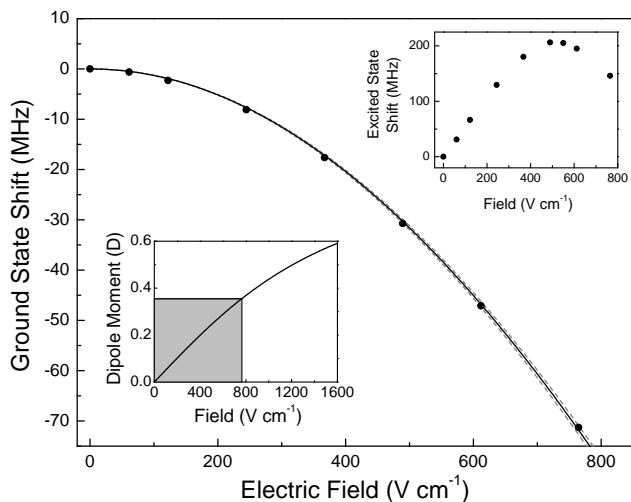


FIG. 4. Stark shift of the rovibrational ground state. The solid black line shows the curve fitted to our results from which we extract a permanent electric dipole moment in the molecular frame of $1.225(3)(8)$ D. The dotted gray lines indicate the upper and lower bounds due to the systematic error in the electric field calculation. Upper inset: Stark shift of the $|\ ^3\Pi_1, v' = 29, J' = 1 \rangle$ excited state used for Stark spectroscopy and STIRAP. The behavior is initially linear with a gradient of approximately $500 \text{ kHz}/(\text{V cm}^{-1})$ up to a field of $\sim 400 \text{ V cm}^{-1}$. Lower inset: Ground-state electric dipole moment in the laboratory frame as a function of electric field. The gray region indicates the range of electric dipole moments currently accessible in the experiment.

of the rigid-rotor Stark Hamiltonian in the laboratory frame [36]. We find a permanent electric dipole moment in the rovibrational ground state of $1.225(3)(8)$ D. The first uncertainty is statistical and the second is systematic, arising from the uncertainty in the electric field [36]. Takekoshi *et al.* recently reported a measured value of $1.17(2)(4)$ D [33], which agrees with our measurement within their uncertainty. The lower inset in Fig. 4 shows the fitted DC Stark shift converted into the equivalent electric dipole moment in the laboratory frame, and the gray region indicates the dipole moment range currently accessible in the experiment. The maximum laboratory-frame dipole moment we can access is $0.355(2)(4)$ D at an electric field of 765 V cm^{-1} .

Our results complement those reported recently by Takekoshi *et al.* [33]. The two experiments produce a similar number of molecules in the rovibrational ground state, even though Takekoshi *et al.* demonstrate higher STIRAP efficiencies of 90%. A key difference between the two experiments lies in the trap geometry; our work uses a simple 3D optical trap, whereas ref. [33] uses a lattice of 2D pancake-shaped traps. A key feature of our work is that we can apply a larger electric field. This allows measurement of the ground-state dipole moment with smaller uncertainties and the realization of larger laboratory-frame electric dipole moments than in [33].

In conclusion, we have presented high-precision spectroscopy of the ground state of $^{87}\text{Rb}^{133}\text{Cs}$ molecules and demonstrated STIRAP transfer to create a sample of over 1000 molecules in the rovibrational ground state. The binding energy of this state is $hc \times 3811.576(1) \text{ cm}^{-1}$ and the splitting between the $J'' = 0$ and 2 rotational levels of the vibrational ground state is $h \times 2940.09(6) \text{ MHz}$. We have used DC Stark spectroscopy to make a precise measurement of the ground-state permanent electric dipole moment as $1.225(3)(8)$ D, and demonstrate that laboratory-frame dipole moments up to $0.355(2)(4)$ D are accessible in our experiment. We believe that this is the largest dipole moment in the laboratory frame accessible in any ultracold molecule experiment to date. For comparison, in $^{87}\text{Rb}^{133}\text{Cs}$, Takekoshi *et al.* access laboratory-frame dipole moments of ~ 0.03 D [33], whilst in KRb, Ni *et al.* report values up to 0.22 D [22]. This brings the possibility of observing strong dipolar interactions in a stable ultracold molecular gas within reach.

ACKNOWLEDGEMENTS

We acknowledge T. Ogden for his help in developing the STIRAP simulation, D.L. Jenkin, D.J. McCarron and H.W. Cho for their work on the early stages of the project and useful discussions with H.-C. Nägerl and members of his group. This work was supported by the UK EPSRC and by EOARD Grant FA8655-10-1-3033. CLB is supported by a Doctoral Fellowship from Durham University. The data presented in this paper are available on request.

* s.l.cornish@durham.ac.uk

- [1] L. D. Carr, D. DeMille, R. V. Krems, and J. Ye, *New J. Phys.* **11**, 055049 (2009).
- [2] D. S. Jin and J. Ye, *Chem. Rev.* **112**, 4801 (2012).
- [3] M. Lemeshko, R. V. Krems, J. M. Doyle, and S. Kais, *Mol. Phys.* **111**, 1648 (2013).
- [4] S. Ospelkaus, K.-K. Ni, D. Wang, M. H. G. de Miranda, B. Neyenhuis, G. Quémener, P. S. Julienne, J. L. Bohn, D. S. Jin, and J. Ye, *Science* **327**, 853 (2010).
- [5] R. V. Krems, *Phys. Chem. Chem. Phys.* **10**, 4079 (2008).
- [6] V. V. Flambaum and M. G. Kozlov, *Phys. Rev. Lett.* **99**, 150801 (2007).
- [7] T. A. Isaev, S. Hoekstra, and R. Berger, *Phys. Rev. A* **82**, 052521 (2010).
- [8] J. J. Hudson, D. M. Kara, I. J. Smallman, B. E. Sauer, M. R. Tarbutt, and E. A. Hinds, *Nature* **473**, 493 (2011).
- [9] D. DeMille, *Phys. Rev. Lett.* **88**, 067901 (2002).
- [10] L. Santos, G. V. Shlyapnikov, P. Zoller, and M. Lewenstein, *Phys. Rev. Lett.* **85**, 1791 (2000).
- [11] M. A. Baranov, M. Dalmonte, G. Pupillo, and P. Zoller, *Chem. Rev.* **112**, 5012 (2012).
- [12] E. S. Shuman, J. F. Barry, and D. DeMille, *Nature* **467**, 820 (2010).

- [13] M. T. Hummon, M. Yeo, B. K. Stuhl, A. L. Collopy, Y. Xia, and J. Ye, *Phys. Rev. Lett.* **110**, 143001 (2013).
- [14] V. Zhelyazkova, A. Cournol, T. E. Wall, A. Matsushima, J. J. Hudson, E. A. Hinds, M. R. Tarbutt, and B. E. Sauer, *Phys. Rev. A* **89**, 053416 (2014).
- [15] T. Köhler, K. Góral, and P. S. Julienne, *Rev. Mod. Phys.* **78**, 1311 (2006).
- [16] K. M. Jones, E. Tiesinga, P. D. Lett, and P. S. Julienne, *Rev. Mod. Phys.* **78**, 483 (2006).
- [17] C. Chin, R. Grimm, P. Julienne, and E. Tiesinga, *Rev. Mod. Phys.* **82**, 1225 (2010).
- [18] K. Bergmann, H. Theuer, and B. W. Shore, *Rev. Mod. Phys.* **70**, 1003 (1998).
- [19] J. G. Danzl, M. J. Mark, E. Haller, M. Gustavsson, R. Hart, J. Aldegunde, J. M. Hutson, and H.-C. Nägerl, *Nat. Phys.* **6**, 265 (2010).
- [20] F. Lang, K. Winkler, C. Strauss, R. Grimm, and J. Hecker Denschlag, *Phys. Rev. Lett.* **101**, 133005 (2008).
- [21] K.-K. Ni, S. Ospelkaus, M. H. G. de Miranda, A. Pe'er, B. Neyenhuis, J. J. Zirbel, S. Kotochigova, P. S. Julienne, D. S. Jin, and J. Ye, *Science* **322**, 231 (2008).
- [22] K.-K. Ni, S. Ospelkaus, D. Wang, G. Quémener, B. Neyenhuis, M. H. G. de Miranda, J. L. Bohn, J. Ye, and D. S. Jin, *Nature* **464**, 1324 (2010).
- [23] M. H. G. de Miranda, A. Chotia, B. Neyenhuis, D. Wang, G. Quémener, S. Ospelkaus, J. L. Bohn, J. Ye, and D. S. Jin, *Nat. Phys.* **7**, 502 (2011).
- [24] B. Yan, S. A. Moses, B. Gadway, J. P. Covey, K. R. A. Hazzard, A. M. Rey, D. S. Jin, and J. Ye, *Nature* **501**, 521 (2013).
- [25] P. S. Żuchowski and J. M. Hutson, *Phys. Rev. A* **81**, 060703 (2010).
- [26] The trimer formation reactions referred to here are the two-body reactions $2\text{RbCs} \rightarrow \text{Rb}_2\text{Cs} + \text{Cs}$ or $\text{Cs}_2\text{Rb} + \text{Rb}$.
- [27] M. Aymar and O. Dulieu, *J. Chem. Phys.* **122**, 204302 (2005).
- [28] K. Pilch, A. D. Lange, A. Prantner, G. Kerner, F. Ferlaino, H.-C. Nägerl, and R. Grimm, *Phys. Rev. A* **79**, 042718 (2009).
- [29] T. Takekoshi, M. Debatin, R. Rameshan, F. Ferlaino, R. Grimm, H.-C. Nägerl, C. R. Le Sueur, J. M. Hutson, P. S. Julienne, S. Kotochigova, and E. Tiemann, *Phys. Rev. A* **85**, 032506 (2012).
- [30] H.-W. Cho, D. J. McCarron, M. P. Köppinger, D. L. Jenkin, K. L. Butler, P. S. Julienne, C. L. Blackley, C. R. Le Sueur, J. M. Hutson, and S. L. Cornish, *Phys. Rev. A* **87**, 010703 (2013).
- [31] M. P. Köppinger, D. J. McCarron, D. L. Jenkin, P. K. Molony, H.-W. Cho, S. L. Cornish, C. R. Le Sueur, C. L. Blackley, and J. M. Hutson, *Phys. Rev. A* **89**, 033604 (2014).
- [32] M. Debatin, T. Takekoshi, R. Rameshan, L. Reichsöllner, F. Ferlaino, R. Grimm, R. Vexiau, N. Bouloufa, O. Dulieu, and H.-C. Nägerl, *Phys. Chem. Chem. Phys.* **13**, 18926 (2011).
- [33] T. Takekoshi, L. Reichsöllner, A. Schindewolf, J. M. Hutson, C. R. Le Sueur, O. Dulieu, F. Ferlaino, R. Grimm, and H.-C. Nägerl, *ArXiv:1405.6037v1* (2014).
- [34] D. J. McCarron, H. W. Cho, D. L. Jenkin, M. P. Köppinger, and S. L. Cornish, *Phys. Rev. A* **84**, 011603 (2011).
- [35] H. W. Cho, D. J. McCarron, D. L. Jenkin, M. P. Köppinger, and S. L. Cornish, *Eur. Phys. J. D* **65**, 125 (2011).
- [36] See supplementary material for more information about the STIRAP laser setup and transfer modelling, electric field generation and calculation, DC Stark shift calculation and curve fitting, and permanent electric dipole moment error analysis.
- [37] M. Debatin, *Creation of Ultracold RbCs Ground-State Molecules*, Ph.D. thesis, University of Innsbruck (2013).
- [38] Y. Yang, X. Liu, Y. Zhao, L. Xiao, and S. Jia, *J. Phys. Chem. A* **116**, 11101 (2012).
- [39] J. Aldegunde, B. A. Rivington, P. S. Żuchowski, and J. M. Hutson, *Phys. Rev. A* **78**, 033434 (2008).

SUPPLEMENTARY MATERIAL

STIRAP laser setup

The two lasers used for STIRAP are locked to a single cylindrical 10 cm high-finesse plane-concave optical cavity, built from ultra-low-expansion glass (ULE) by ATFilms, housed in a vacuum chamber from Stable Laser Systems and actively stabilised to the zero-expansion temperature of the ULE at 35°C. The properties of the reference cavity are summarised in Table I. Light entering the cavity first passes through a fibre-coupled electro-optic modulator (EOM), adding tunable sidebands at up to 10 GHz which can span the 1.5 GHz free spectral range (FSR) of the cavity. Additional sidebands are added at ~ 10 MHz in order to implement a standard Pound-Drever-Hall lock to the cavity. By locking to a sideband instead of a fundamental mode, we can tune the laser frequency continuously between the cavity modes. We measure the FSR of the reference cavity to ± 1 kHz by locking to a TEM₀₀ mode and scanning the driving frequency of the fibre EOM across the adjacent TEM₀₀ mode, monitoring the change in the cavity transmission in the process. Such precise knowledge of the FSR is important for the measurements of the rotational splitting of the ground vibrational state of the $^{87}\text{RbCs}$ molecule. The absolute optical frequencies of both lasers are measured with a commercial wavemeter, calibrated with the $5\text{P}_{3/2} \leftrightarrow 4\text{D}_{5/2}$ transition in Rb at 196 THz.

Test wavelength (nm)	977	1557
Zero-expansion (°C)	35	—
Length (mm)	100.13958(7)	100.15369(7)
FSR (MHz)	1496.873(1)	1496.662(1)
Finesse	$1.37(6) \times 10^4$	$1.19(6) \times 10^4$
Mode linewidth (kHz)	109(5)	126(5)

TABLE I. Properties of the optical cavity used to narrow the linewidths of the STIRAP lasers.

Fixed frequency (80 MHz) acousto-optic modulators provide continuous adjustment of the power of each of the STIRAP beams. The beams are coupled through 8 m fibres to the main experiment, collimated and overlapped on a dichroic mirror. The pump and Stokes beams are then focussed by a single achromatic lens to overlapped $37(1) \mu\text{m}$ and $35.3(6) \mu\text{m}$ spots respectively at the molecular sample.

STIRAP transfer modelling

We model the transfer using a four-level scheme as shown in Fig. 1. The Feshbach state $|F\rangle$, excited state $|E\rangle$ and ground state $|G\rangle$ are coupled by two Rabi frequencies $\Omega_P(t)$ and $\Omega_S(t)$ describing the pump and Stokes fields, respectively. Loss of population from the system

due to the non-adiabaticity of the transfer is modelled as a decay of $|E\rangle$ to a dump level $|X\rangle$ at the rate determined by the natural linewidth of the excited state, γ . We are currently unable to measure the out-of-loop laser noise directly and therefore do not include it in the model. We build this system using the QuTiP module in Python [1], and numerically integrate the Lindblad master equation. $\Omega_P(t)$ and $\Omega_S(t)$ are calculated from an analytic approximation of the measured response of the beam modulators and the maximum Rabi frequencies. $\Omega_{P,\text{max}}$ is measured as explained in the main text, while $\Omega_{S,\text{max}}$ is fitted as a free parameter. The round-trip transfer is taken as the simulated population of the $|F\rangle$ state at the end of the ramp sequence.

We observe that the proximity of the $\lambda = 1550$ nm trapping lasers to the pump transition at $\lambda = 1557$ nm produces a large AC Stark shift. We also note there is considerable broadening of the pump transitions to greater than 1 MHz, which may be attributable to the variable Stark shift across the cloud. In our models and calculations we therefore use the 130 kHz natural linewidth measured by Takekoshi *et al.* [2].

Electric field creation and calculation

The electric field is generated by a set of four electrodes running parallel to the outside of the fused silica cell. The electrodes are 1.5 mm in diameter, separated by 29.0(2) mm vertically, 24.8(2) mm horizontally and are 22.0(5) mm long. They are bent at either end at a radius of 2(1) mm to allow electrical connections to be made without interfering with the already limited optical access to the cell. The electrodes are currently connected in pairs so that the two electrodes above the cell are negatively charged, and the two below the cell are positively charged. We do not currently have any experimental method of calibrating our electric field. We therefore calculate the electric field at the center of the cell by the method of finite element analysis to solve the Poisson equation. A 3D mesh is generated from a CAD model of the experimental apparatus

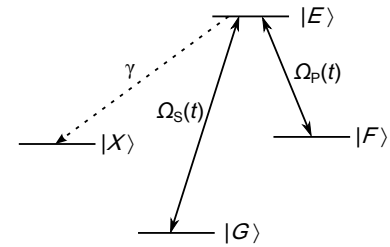


FIG. 1. Level scheme used in the ground state transfer model. Solid lines are driven transitions, dashed lines are radiative decays.

which includes the electrodes, cell walls, earthed magnetic field coils, and dielectric coil mounts. The mesh creation and subsequent calculation is carried out in the Autodesk Multiphysics software package. It is found that the presence of the fused silica cell (external dimensions of 24 mm \times 24 mm \times 80 mm, with 2 mm thick walls) enhances the electric field by $\sim 2\%$. The electric field at the center of the cell given an applied electric potential of 1 kV between the upper and lower electrode pairs is 153(1) V cm $^{-1}$. The gradient of the electric field at the center of the cell is zero, so the uniformity is determined by the curvature of the field as defined by its second order derivative equal to 17(5) V cm $^{-3}$. Hence a displacement of the molecular cloud from the center of the cell by 1 mm leads to a variation in the electric field seen by the molecules of less than 0.1 %.

The high voltage power supplies connected to the electrodes are TTL controlled so that the field is only applied for the portion of the experiment when the STIRAP pulses are in operation. It is important for the accurate calculation of the electric field that we avoid electric polarization of our cell. We find experimentally that polarization of our cell starts to become detectable at ~ 1 kV cm $^{-1}$. Above this critical field we are able to observe a remnant electric field with inverse polarity to that previously applied, this causes a Stark shift of the pump and Stokes transitions even when the electric field is switched off. We therefore do not make any measurements above 765 V cm $^{-1}$. In addition we have measured the Stark shift of the excited state at 245 V cm $^{-1}$ with the electric field applied in the reverse direction. We measured a 50 kHz disparity between forward and reverse field Stark shift measurements, against an overall Stark shift for the transition of 130 MHz. Remnant polarization can remain in the experiment for days following a high voltage pulse. To remove this polarization between measurements, we bathe the cell in UV light. The UV light is generated by a single LED (Roithner-Lasertechnik LED395-66-60-110), and has a typical output power of 240 mW at 395 nm.

Calculation of the fitted ground state DC-Stark shift

Fitting of the ground-state DC-Stark shift is done by calculating the matrix elements of the relevant rigid rotor Stark Hamiltonian. These matrix elements are defined by

$$\begin{aligned} \langle J \ m_J | H | J' \ m_J' \rangle &= B_0 \cdot J(J+1) \cdot \delta_{JJ' m_J m_J'} \\ &- d_0 E \sqrt{(2J+1)(2J'+1)} \cdot (-1)^{m_J} \cdot \\ &\quad \begin{pmatrix} J & 1 & J' \\ -m_J & 0 & m_J' \end{pmatrix} \begin{pmatrix} J & 1 & J' \\ 0 & 0 & 0 \end{pmatrix}, \quad (1) \end{aligned}$$

where J and m_J are the rotational quantum numbers and its projection along the z axis respectively, B_0 is our experimentally measured rotational constant, E is the applied electric field, and the two matrices are Wigner 3-j coefficients. We include rotational levels up to $J = 8$. This equation can be understood by considering its two terms separately. The first is the rotational splitting without the presence of an applied field, the second is the DC-Stark shift.

Systematic error budget for experimentally measured permanent electric dipole moment in the lab frame

The major sources of systematic error in the calculated value of the permanent electric dipole moment can be seen in Table II. They are broken down into three areas. The first is due to the uncertainty in the measurement of the electrode separations, including any uncertainties in the electrode shape (i.e. the bend radius at either end of each electrode). The next source of error is caused by the uncertainty in the position of the molecular cloud with respect to the center of the electrode array. This uncertainty is estimated to be ± 1 mm in any direction. Note that the position of the glass cell with respect to the electrode array has an error of similar magnitude. However, calculations of the electric field where we move the glass cell by ± 1 mm show negligible deviation from the central value. The final source of error is from the electric field calculation itself. Finite element analysis is an approximate method which relies upon a converging solution. This convergence has some noise, which is estimated by repeating the calculation with a various mesh densities. We estimate the uncertainty in this value to be $\pm 0.7\%$ of the central electric field at a given potential. It is clear that the uncertainty is dominated predominantly by the accuracy of the measurement of the electrode position.

	α_{d_0} (D)
Electrode separation	± 0.007
Molecule position	± 0.002
Field calculation	± 0.004
Total systematic error	± 0.008

TABLE II. Breakdown of the various sources of systematic uncertainty in the measured value of the permanent electric dipole moment (α_{d_0}).

- [1] J. Johansson, P. Nation, and F. Nori, Computer Physics Communications **183**, 1760 (2012).
- [2] T. Takekoshi, L. Reichsöllner, A. Schindewolf, J. M. Hutson, C. R. Le Sueur, O. Dulieu, F. Ferlaino, R. Grimm, and H.-C. Nägerl, ArXiv:1405.6037v1 (2014).